ORIGINAL ARTICLE

FFEMS — Fatigue & Fracture of Engineering Materials & Structures   WILEY

Fatigue properties of a structural rotor blade adhesive under axial and torsional loading

Michael Kuhn[1] [iD] | Nikolas Manousides[1] | Alexandros Antoniou[2] | Claudio Balzani[1]

[1]Institute for Wind Energy Systems, Leibniz University Hannover, Hannover, Germany

[2]Institute for Wind Energy Systems, Fraunhofer IWES, Bremerhaven, Germany

Correspondence
Michael Kuhn, Institute for Wind Energy Systems, Leibniz University Hannover, Appelstraße 9A, 30167 Hannover.
Email: research@iwes.uni-hannover.de

Abstract

Axial and torsional fatigue tests at different stress ratios were performed on a structural adhesive designed for wind turbine rotor blades. By employing previously optimized specimens, fatigue properties were recorded without influences of manufacturing-induced defects such as pores. The Stüssi S–N model was an excellent fit to the data and was combined with a Haibach extension line to account for uncertainties in the gigacycle fatigue regime. A comparison of the results with hand-mixed specimens revealed significant and load level-dependent differences, indicating that manufacturing safety factors should be applied to the slope of the S–N curve. The experiments were accompanied by stiffness degradation measurements, which enabled an analysis of Young's and shear modulus degradation interactions. The degradation was modeled using power law fits, which incorporated load level-dependent fitting parameters to allow for a full description of the stiffness reduction and a prediction of the residual fatigue life of run-out specimens.

KEYWORDS
multiaxial fatigue, porosity, stiffness degradation, structural adhesives, wind turbine rotor blades

1 | INTRODUCTION

In order to assure the structural reliability of a material in cyclic loading conditions, experimental fatigue tests have to be conducted. This way, the dependence of the material properties on the load level and the cycles to failure can be established. In most cases, this is done with coupon specimens whose results are transferred to the analysis of more complex structures. Hence, coupon level fatigue tests are most representative for these structures if the manufacturing and general processing of the respective material is done in a comparable way for the coupon specimens and the final structure.

1.1 | Fatigue in bond lines of wind turbine rotor blades

In the manufacture of wind turbine rotor blades, two aerodynamic half shells and multiple shear webs are joined using structural adhesives. On account of the size of the separate parts, the adhesive also serves as a mitigation for

manufacturing tolerances. Therefore, the bond line geometry varies along the length of the blade, with common thickness variations between 10 and 15 mm.[1–3]

In addition to challenges in the manufacturing process, wind turbine rotor blades are exposed to very high fatigue loads. The rotation of the rotor imposes a varying gravitational load, which is superimposed by a stochastic wind load leading to complex multiaxial loads over a lifetime of at least 20 years.[4–6]

Given the high fatigue loads of rotor blades, a reliable characterization of the fatigue properties of the employed materials is of utmost importance. As the reliability of fatigue data directly impacts the applicable safety margins in the blade design, this greatly impacts the optimization potential as well. In addition, the advent of digital twins of rotor blades requires well-known margins of the material properties.[1,7,8]

1.2 | Experimental investigations of bond line fatigue

Although the adhesive application in rotor blade manufacturing is done using dosing machines,[3] which generally involves a vacuum-based mixing process, most publications on the mechanical properties of rotor blade adhesives are based on hand-mixed specimens.[2,9–11]

Due to high porosity levels attributed to hand-mixing, the derived material properties are diminished and are not representative for modern rotor blade manufacture. In a recent publication,[12] the porosity level of hand-mixed coupon specimens was compared with machine-mixed ones utilizing μCT scans. In a comparison with a scan of cured adhesive inside a conveyor hose of an industrial dosing and dispensing machine, it was found that the machine-mixed specimens had a comparable porosity level, while the quality of the hand-mixed specimens was insufficient to represent the industrial standard. In terms of material properties, it was proven that the ultimate static strength in tension of hand-mixed specimens was 33% less than that of machine-mixed specimens with negligible porosity. The plastic strain increased by a factor of 5.28, so that hand-mixed specimens could be classified as brittle while machine-mixed specimens were rather ductile. At the same time, the scatter of the static material properties drastically decreased for machine-mixed specimens in comparison with the hand-mixed ones; for example, the coefficient of variation of the tensile failure strength was 1.21% for the machine-mixed specimens while it was up to 12.92% for the hand-mixed ones. Since the scatter of fatigue tests can be expected to be much larger than in static tests, fatigue tests with hand-mixed specimens will lead to much more conservative and unreliable data sets.

Additionally, data on the stiffness degradation are scarce. However, since these data enable more comprehensive material modeling, they are a valuable byproduct of fatigue tests. A reliable stiffness degradation model might also be useful to estimate the residual fatigue life of run-out specimens. If the degradation is non-linear, the modeling of sequence effects in the fatigue life prediction might also be possible.

Note that the transfer of mechanical properties of (bulk) adhesive specimen to the joint and interface scale is not trivial due to manufacturing related effects resulting from the application and curing process (degree of polymerization, exothermicity, and residual stresses).[12–15] However, testing virtually defect free coupon specimens allows for a pristine material characterization, which in turn enables the quantification of effects of defects such as pores with additional (lower quality) coupon specimens or joint scale tests. This way, safety factors can be adapted to different manufacturing techniques, for example, in rotor blade manufacture, where pores might still occur due to the application process of the adhesive and reinforcement fibers within the adhesive might be aligned differently.

1.3 | Aims and outline

Since most contributions to the analysis of rotor blade bond line fatigue were based on hand-mixed specimens, compare Section 1.2, the scatter of the results might be governed by manufacturing imperfections. Therefore, it is difficult to derive fatigue properties of the material itself. This might also render the validation of damage prediction models impossible, especially in case of more complex multiaxial loading scenarios.

In order to derive more reliable fatigue properties, the optimized specimens from a previous study[12] are used in this work. These specimens allow for a fatigue characterization in both axial and torsional loads, while being virtually free of imperfections such as porosities. Separate specimens for different load scenarios are also not required, and possible stress concentration issues with different specimen geometries are prevented.

Section 2 summarizes the specimen manufacturing and testing conditions. The results of uniaxial fatigue tests and corresponding curve fits are shown in Section 3 followed by stiffness degradation measurements in Section 4.

2 | SPECIMENS AND FATIGUE TEST SETUP

The manufacturing of the utilized specimens and fatigue testing conditions are briefly explained in the following.

FE Optimized Geometry
Parametric study to minimize stress concentrations and to assure failure in the test section

Optimized Manufacturing
Vacuum speed mixing combined with 3D printed mould inserts and injection moulding for high homogeneity and low porosity

Fatigue Test
Instrumentation: Pt100 for surface temperature measurement

Residual Strength Test
Instrumentation: low elastic stain gauge rosettes for polymers

FIGURE 1 Test setup for every fatigue test conducted. A Pt100 sensor is used to measure the surface temperature. In case a run-out is declared, a residual strength test is performed using strain gauge rosettes.[16] Optimization processes related to the specimen geometry and manufacturing were presented in a previous publication.[12] Dimensions in mm. [Colour figure can be viewed at wileyonlinelibrary.com]

FIGURE 2 Qualitative porosity comparison of the specimens used for this study. Pores are indicated in red. The specimen numbers are given left of the respective depictions. The specimens are sorted according to the respective cycles to failure shown in Table 1. [Colour figure can be viewed at wileyonlinelibrary.com]

2.1 | Material system and manufacturing

The specimens used for the experiments in this work were made of EPIKOTE™ Resin MGS™ BPR 135G3 mixed with EPIKURE™ Curing Agent MGS™ BPH 137G.[12] The material is a structural adhesive and commonly used in the wind energy industry. It is epoxy-based and short glass fiber-reinforced.[17]

The tubular and tapered geometry of the specimens, compare Figure 1, was optimized in a parametric study based on finite element analyses, while the manufacturing employed vacuum speed mixing in combination with 3D printed mold inserts in an injection molding process. Details concerning the manufacturing process can be found in a dedicated paper.[12]

To verify the manufacturing quality regarding the porosity and mixing homogeneity, high-resolution X-ray microscopy (μCT scanning) was employed using a Zeiss Xradia 410 Versa.[18] The scans required for this work are depicted in Figure 2 and show that the porosity is negligible close to the test section. It should be noted that the scans did not allow for an analysis of the orientation of the reinforcement fibers as the voxel size was limited to approximately 32 μm. This will be done in a future work. An anisotropy of the specimens was, however, confirmed by analogy of the stiffness in axial and torsional direction.[12] A primarily axial orientation of the reinforcement fibers is likely.

2.2 | Fatigue test setup

A servohydraulic Walter + Bai LFV 100-T2000 was used for the experiments, which has independent control of axial and torsional loads.[19] In combination with tubular specimens, the independency of the load application allows for versatile tests, which are not feasible with, for example, arcan fixtures.

Since the measurement campaign of this work is based on a polymer, which was proven to show viscoelastic behavior,[20] in situ temperature measurements were conducted with Pt100 sensors attached to the surface of the specimens as shown in Figure 1. In order not to increase the specimens temperature too much (approximate limit: +5 K above ambient temperature), the test frequencies were adjusted at each load level. Simultaneously, the test frequency adaption lowers viscoelastic effects since the strain rate is more similar on the respective load levels than in tests with constant test frequencies.

The stiffness degradation measurements were inspired by Adden and Horst[21] and consisted of repeated displacement-controlled steps in axial and torsional direction. The amount of measurement repetitions resulted from a fixed number of cycles in between the degradation characterization steps. It was adjusted in such a way that the stiffness degradation could be modeled with at least 50 individual measurements for each specimen to assure a sufficient resolution of the data. Since the respective displacements were very small and approximately the same as in static stiffness measurements, for example, corresponding to 2000 μm/m in axial direction, these additional measurements have negligible effect on the fatigue life. In addition, the load–displacement curve is approximately linearly proportional to the stress–strain curve at these displacement levels. Therefore, the stiffness degradation can be approximated without additional strain gauges or other measurement devices, reducing the experimental effort. A flow chart of the employed stiffness degradation measurement is shown in Figure 3.

All fatigue tests were intended as load-controlled tests. However, due to a problem with the inertia compensation of the torsional load cell, torque-control was
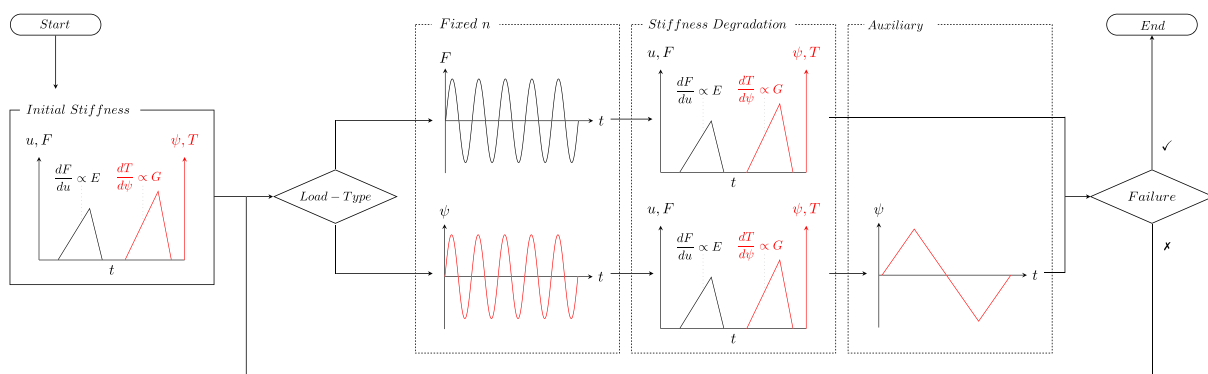

FIGURE 3 Flow chart of the stiffness degradation measurement in both axial and torsional direction to identify E and G modulus degradation. Degradation measurements are implemented as displacement-controlled steps and repeated after a fixed number of cycles n. [Colour figure can be viewed at wileyonlinelibrary.com]

not possible at the usual fatigue testing frequencies. Therefore, the torsional fatigue tests had to be performed in displacement control instead. To be able to convert the displacement-based results to stress-based results in a postprocessing step, a very slow auxiliary cycle was implemented after the stiffness degradation step; see Figure 3. Since the displacement rate of this cycle matched the one of the static tests, the torque measurement for this cycle was reliable. Details of the conversion will be discussed in Section 3.2.

3 | UNIAXIAL S–N CURVES

Fatigue data in this work were measured in both axial and torsional directions at a stress ratio $R = -1$, defined as the ratio of minimum and maximum stress:

$$R = \frac{\sigma_{\min}}{\sigma_{\max}}. \tag{1}$$

To investigate the effect of a mean stress on the fatigue life, an additional axial S–N curve was recorded at $R = 0$. In all cases, the stiffness degradation measurement was included as described in Section 2.2.

3.1 | S–N models

Since the inception of fatigue tests by Wöhler,[22] many S–N curve descriptions have been proposed. The approach by Basquin[23] is among the most widely used models. It predicts an exponential relationship between the stress amplitude σ_a and the load cycles N and is given by

$$\sigma_a = \alpha N^\beta. \tag{2}$$

Therein, α and β are curve fitting parameters. While the Basquin approach is popular due to its simplicity, it also tends to be non-conservative in the low cycle fatigue (LCF) regime and too conservative in the very high cycle fatigue (VHCF) regime.

The non-conservatism of the Basquin approach in the LCF regime was solved by Sendeckyj[24] who proposed an asymptotic behavior of the S–N curve towards the ultimate static strength R_m expressed by

$$\sigma_a = \frac{R_m}{(1 - \alpha + \alpha N)^\beta}. \tag{3}$$

To account for both the LCF and the VHCF issues of the Basquin approach, different (inverse) sigmoidal-shaped S–N curves have been proposed. One of them is the Stüssi[25] S–N formulation given by

$$\sigma_a = \frac{R_m + \alpha N^\beta \sigma}{1 + \alpha N^\beta}, \tag{4}$$

where σ is the fatigue limit amplitude, which is often also referred to as the endurance limit. A more recent approach was proposed by Kohout and Věchet,[26] which can be formulated as follows:

$$\sigma_a = \sigma \left(\frac{N + \alpha}{N + \gamma} \right)^\beta, \tag{5}$$

where γ is another curve fitting parameter.

The curve fitting parameters α, β, γ, and σ of the S–N approaches can be obtained via a non-linear least squares optimization. The minimization function can utilize the stress-based formulations or the rearranged cycle-based formulations. As each of these minimization strategies can lead to different curve fitting parameters, the parameters from the best overall curve fit or the more conservative resulting S–N curve can be chosen.

Note that in this work the ultimate static strength R_m corresponds to $N = 0.25$ for the S–N modeling, since a static tests can be interpreted as the first quarter of a full cycle.

3.2 | Conversion from displacement to load control

On account of the displacement-controlled torsional fatigue tests, the applied torque is not constant but a collective. The approximation of this collective was done via auxiliary steps in the stiffness degradation routine, compare, Figure 3. The peak values of these auxiliary cycles matched the fatigue amplitude and allowed the construction of torque-collectives in a post-processing step; two of those are shown on the left of Figure 4.

The mean torque-collectives of all load levels were subsequently converted into shear stress collectives using the relationship of torque T and shear stress τ measured in the static tests.[20] Strain rate effects in the fatigue tests might alter the T/τ-relationship of the static tests, but since the displacement rate of the auxiliary cycle was the same as in the static tests, this is expected to be a valid engineering approximation. As an increase in strain rate usually coincides with higher peak stresses, this procedure is also expected to be conservative when it is based on the slow strain rates of static tests. However, strain
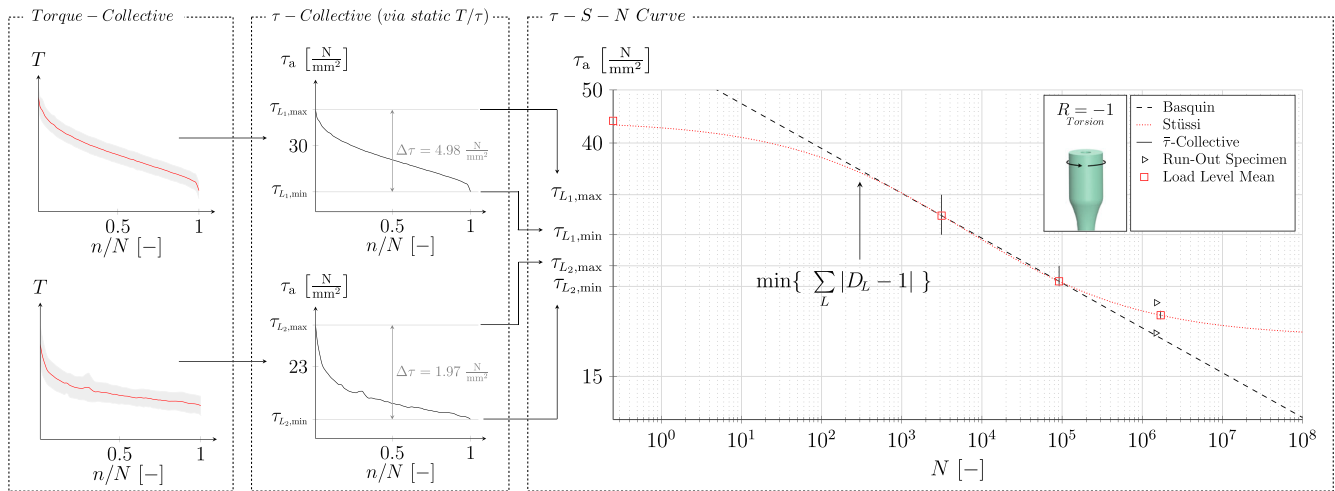
FIGURE 4 Conversion steps from displacement (rotation angle) controlled data to a τ-S–N curve. Torque collectives are generated via auxiliary measurements, compare Figure 3, and converted to shear stress collectives via the relationship of torque and shear stress measured in static tests.[20] The shear collectives form a vertical line in the S–N diagram, which is the basis for a damage-based optimization to find the best-fit S–N curves. [Colour figure can be viewed at wileyonlinelibrary.com]

rate effects of the adhesive are yet to be validated in future experiments.

The mean τ-collectives were subsequently transferred to the S–N diagram, leading to a vertical line for each investigated load level. The linear damage accumulation rule[27] was assumed to be valid in order to fit S–N curves to the data. Based on this assumption, an optimization was set up, which minimized the damage difference to the ideal value of $D = 1$ at each load level. The best-fit results of the S–N models according to Basquin and Stüssi are shown on the right of Figure 4. Given that the damage-equivalent amplitude of the first load level is approximately the mean value of the respective τ-collective seems plausible as this collective is close to being linear. Likewise, it is reasonable that the damage-equivalent amplitude of the second load level is within the lower third of the respective collective, which decreases rapidly at first and transitions into a slow linear decline.

With respect to the assumptions explained above, the described conversion methodology is expected to be an accurate and conservative approximation for engineering purposes.

3.3 | Experimental results

The results of the fatigue tests are shown in Figure 5 and Table 1. It can be observed that the Basquin S–N curve is expectedly non-conservative in the LCF regime and too conservative in the VHCF regime for all stress ratios and load types. Deviations of the experimental data to the

Basquin S–N curve start from approximately 100,000 to 200,000 cycles in each case.

Both the Stüssi- and the Kohout-Věchet S–N curves fit the experimental data very well. A deviation of these approaches to one another is only visible in the LCF and VHCF regime, whereas the Stüssi approach is more conservative in both cases and is hence interpreted as the best-fit. The Sendeckyj S–N curve matches the Kohout–Věchet approach in the LCF regime and is similar to the Basquin line afterwards.

The experimental results are also summarized in Table 1. The test frequency was varied in order to limit internal heating of the specimens and strain rate effects. In most cases, the temperature increase in comparison with the ambient temperature was below 3 K. However, some specimens reached 4–6.65 K, which was most probably caused by friction between the Pt100 and the specimen due to an insufficient fixture of the sensor, as other specimens did not heat up as much in the same testing conditions. Slight variations of the measured temperatures may have been caused by minor positioning differences of the Pt100 on the tapered specimens. Nevertheless, it is expected that the average temperature increase during the experiments has a negligible effect on the fatigue life. Minor variations of the stress amplitudes within each load level resulted from very small cross-sectional differences of the specimens in addition to minimal changes of the load amplitude on account of the testing machine controller.

The S–N fitting parameters can be found in Table 2. On account of the different S–N formulations, the
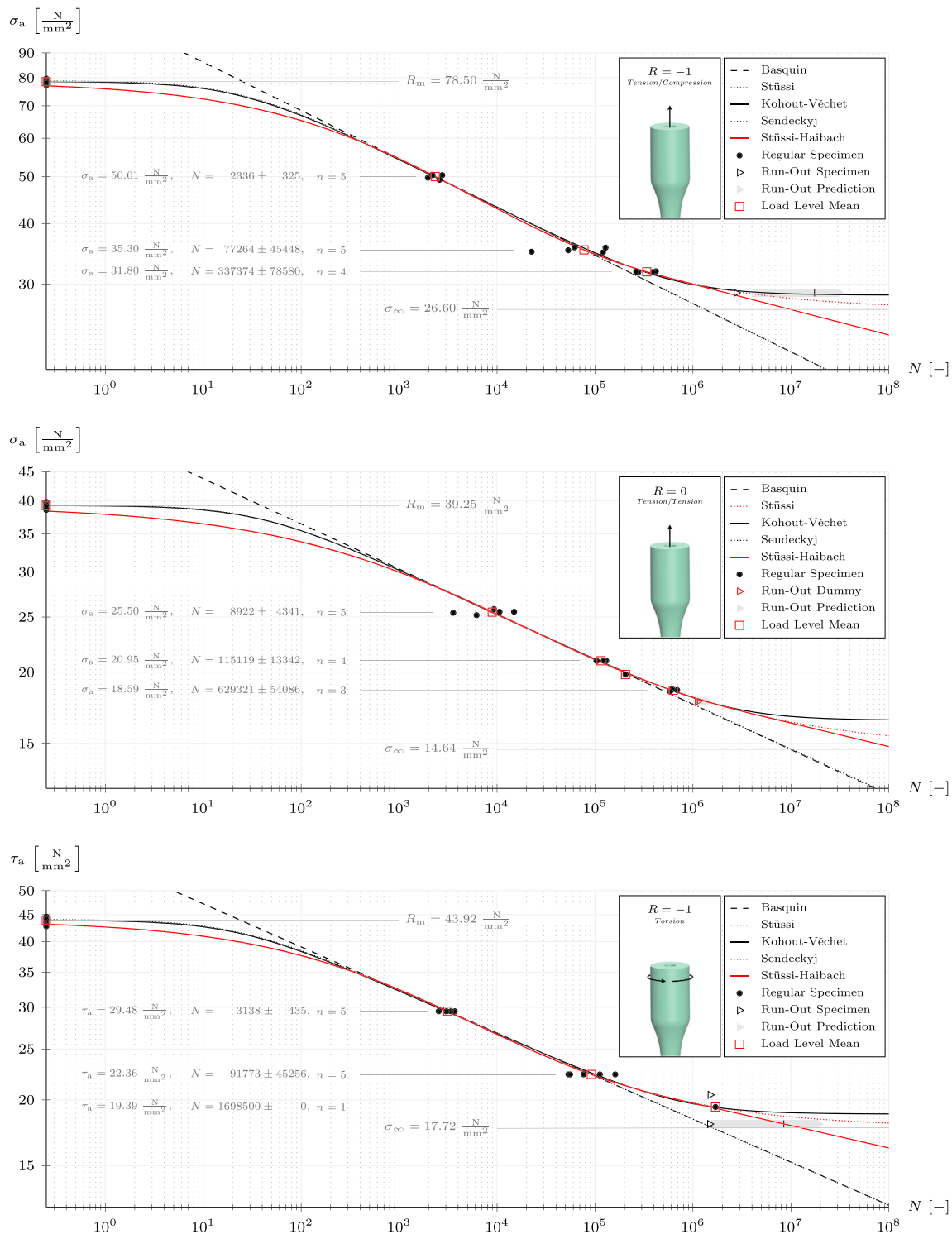
FIGURE 5 S–N curves for tension/compression, tension/tension and torsion with corresponding load level mean values and static strength R_m. The fatigue limit σ is based on the respective Stüssi S–N curve fit. The number of failed specimens of a load level is indicated by n. [Colour figure can be viewed at wileyonlinelibrary.com]

parameters cannot be easily compared with each other. The applied Haibach extension will be discussed in Section 3.4.

In total, four specimens were excluded from the S–N fits. Specimen 042 was accidentally preloaded in tension during clamping due to very tight tolerances of the

TABLE 1 Summarized fatigue results for all experiments conducted.

Load type	Specimen no.	σ_a [N/mm^2]	τ_a [N/mm^2]	N [−]	f [1/s]	ΔT_{max} [K]	$\tilde{E}_f$ [%]	$\tilde{G}_f$ [%]
$\sigma_a^{R=-1}$	177	49.73	−	1970	1.0	2.72	88.5	95.9
	051	50.43	−	2164	1.0	2.79	88.1	96.1
	183	50.33	−	2202	1.0	3.07	86.4	93.1
	171	49.24	−	2587	1.0	4.22	85.3	93.3
	136	50.35	−	2759	1.0	3.71	88.1	95.5
	010	34.99	−	22531	3.0	0.58	91.2	96.9
	114	35.23	−	53261	3.0	4.15	87.0	95.0
	189	35.72	−	61858	3.0	1.00	85.4	93.6
	007	34.87	−	120433	3.0	3.87	91.4	97.3
	194	35.68	−	128148	3.0	4.07	85.5	95.5
	203	31.82	−	263633	3.0	2.47	88.4	95.6
	054	31.73	−	276747	3.0	2.61	91.9	96.9
	139	31.76	−	390704	3.0	3.32	91.4	96.7
	094	31.88	−	418412	3.0	3.32	91.1	98.0
	174	28.79	−	*2760000	3.0	1.94	93.7	99.5
$\sigma_a^{R=0}$	154	25.43	−	3568	1.0	1.06	96.9	98.4
	169	25.19	−	6179	1.0	0.63	95.2	97.9
	207	25.82	−	9322	1.0	0.75	95.4	97.1
	199	25.53	−	10606	1.0	0.93	96.5	97.4
	026	25.54	−	14937	1.0	0.40	97.7	98.2
	112	20.98	−	103500	3.0	1.63	98.2	100.9
	193	20.92	−	104284	3.0	1.94	96.5	97.9
	069	20.95	−	122507	3.0	1.52	96.1	100.0
	198	20.94	−	130186	3.0	1.71	97.4	99.7
	042	20.89	−	+346500	3.0	0.89	96.2	98.0
	106	19.82	−	204793	4.0	1.53	98.7	98.6
	167	18.50	−	e345000	4.0	−	−	−
	110	18.49	−	585123	4.0	1.76	96.5	99.2
	108	18.67	−	613208	4.0	2.00	97.5	−
	099	18.60	−	689632	4.0	1.64	95.5	98.6
$\tau_a^{R=-1}$	089	−	29.48	2536	0.5	1.28	95.7	84.3
	186	−	29.48	3015	0.5	1.00	94.2	85.1
	123	−	29.48	3057	0.5	3.23	93.2	81.7
	197	−	29.48	3383	0.5	2.19	96.0	83.5
	077	−	29.48	3697	0.5	1.95	95.8	84.0
	083	−	22.36	53607	1.5	2.41	94.0	90.0
	179	−	22.36	55661	1.5	3.45	93.8	86.6
	192	−	22.36	76596	1.5	5.46	93.8	88.1
	173	−	22.36	112000	1.5	4.36	94.7	85.8
	072	−	22.36	161000	1.5	2.24	96.4	90.5
	084	−	20.37	f30000	3.0	−	−	−
	059	−	20.37	f134000	3.0	6.65	95.6	90.5
	057	−	20.44	*1500000	3.0	4.34	97.9	87.4

TABLE 1 (Continued)

Load type	Specimen no.	σ_a [N/mm²]	τ_a [N/mm²]	N [−]	f [1/s]	ΔT_{max} [K]	$\tilde{E}_f$ [%]	$\tilde{G}_f$ [%]
	119	−	19.39	1698500	3.0	4.18	100.1	91.9
	166	−	17.99	*1480000	3.0	2.96	96.5	91.9

Note: Therein, f is the test frequency, ΔT_{max} is the maximum temperature difference to the ambient temperature, and $\tilde{E}_f$ and $\tilde{G}_f$ correspond to the relative stiffness degradation before failure. Run-out specimens are indicated with superscript *. Nontypical fracture surfaces are marked by a superscript f. Specimen 042, also marked with a superscript $+$, was accidentally preloaded during clamping. The superscript e marks a worst-case estimate due to a data recording error. All superscripts refer to the N column.

TABLE 2 Fitting parameters of all S–N models used in this work.

Load type	Model	α [−]	β [−]	γ [−]	σ [N/mm²]	R_m [N/mm²]	N_{ext} [−]	$\sigma_{a,ext}$ [N/mm²]	β_{ext} [−]
$\sigma_a^{R=-1}$	Basquin	108.3051	−0.0996	−	−	−	−	−	−
	Sendeckyj	0.0392	0.0997	−	−	78.5026	−	−	−
	Stüssi	0.0538	0.4022	−	26.6030	78.5026	530,000	31.0088	−0.0524
	Kohout-Věchet	24.4363	−0.0996	651,716.72	28.4735	−	−	−	−
$\sigma_a^{R=0}$	Basquin	52.5354	−0.0793	−	−	−	−	−	−
	Sendeckyj	0.0263	0.0789	−	−	39.2513	−	−	−
	Stüssi	0.0590	0.3367	−	14.6433	39.2513	3,860,000	16.9343	−0.0413
	Kohout-Věchet	37.9438	−0.0793	2,174,478.52	16.4639	−	−	−	−
$\tau_a^{R=-1}$	Basquin	56.9826	−0.0819	−	−	−	−	−	−
	Sendeckyj	0.0412	0.0819	−	−	43.9170	−	−	−
	Stüssi	0.0515	0.3939	−	17.7151	43.9170	630,000	20.1167	−0.0427
	Kohout-Věchet	22.9564	−0.0819	735,298.70	18.8014	−	−	−	−

Note: R_m was determined in a previous publication.[20] Note that α is in N/mm² for the Basquin model and dimensionless for the others. The intersection point of the Stüssi and Haibach line is given by (N_{ext}, $\sigma_{a,ext}$).

specimen and the clamping gear. The preload was estimated to 51 N/mm², which is above the yield point of 39.32 N/mm² and therefore led to strain hardening,[20] causing the fatigue life to approximately triple compared with the other specimens at the same load level, compare Table 1. Specimen 059 and 084 had a significantly lower fatigue life while also showing a fragmented fracture pattern, which was very different from the usual case of a governing 45° crack in torsion, compare Figure 6. Handling errors during the manufacturing (e.g., during demolding or grinding) are suspected to have caused precracks in these specimens. A data recording error caused the exclusion of specimen 167. The cycle to failure of this specimen is a worst-case estimation based on the approximate machine run time.

In four cases, the fatigue test had to be aborted, and a run-out was declared as the total number of cycles of the whole testing campaign was limited. All of these specimens were destroyed in residual strength tests, which are discussed in Section 4 alongside a residual fatigue life prediction based on the stiffness degradation measurements.

Note that the presented results may differ for other test frequencies than the applied ones due to the viscoelastic behavior of the adhesive[20] and associated strain rate effects.

3.4 | Engineering approach to gigacycle fatigue

As (very) high-frequency fatigue testing machines, for example, piezoelectric or rotary bending machines, made experimental fatigue tests beyond 10^7 cycles possible from an economical point of view, the existence of a fatigue limit σ was discussed by several researchers.[28–31]

It was found that multiple materials indeed show a plateau of fatigue strength in between 10^6 and 10^7 cycles,
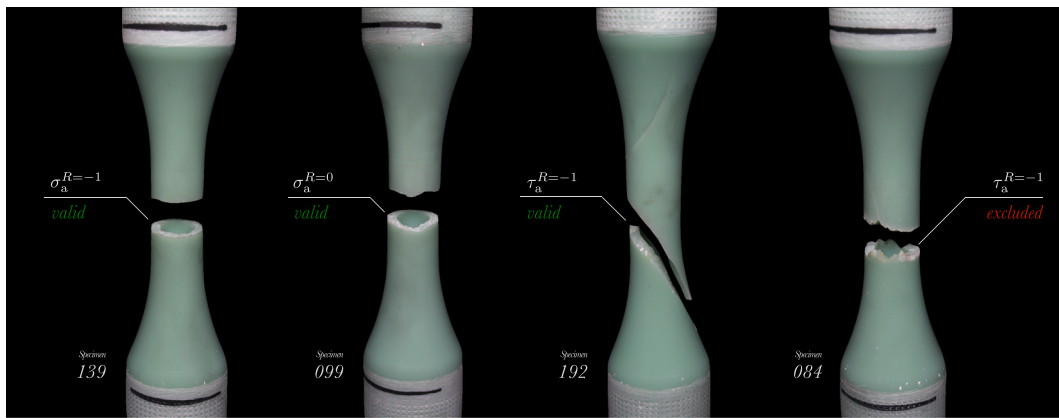
FIGURE 6 Typical fracture patterns in the fatigue tests for all investigated load types. Specimen 084 was excluded from the analysis due to an atypical fracture pattern, which was probably caused by precracks on account of handling errors in the manufacturing process. [Colour figure can be viewed at wileyonlinelibrary.com]
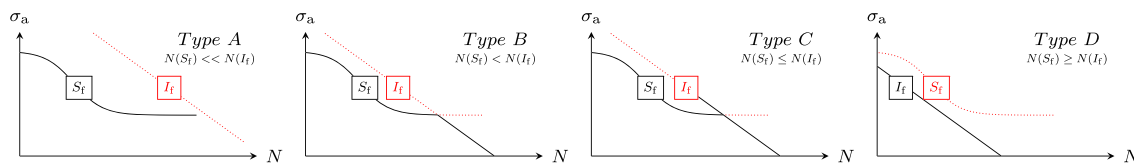

FIGURE 7 Gigacycle fatigue types depicted in double logarithmic axes. Depending on the material, the fatigue life can be dominated by surface-induced failure S_f, internal damage initiation I_f, or mixtures of both phenomena. Adapted from Shiozawa et al.[28] [Colour figure can be viewed at wileyonlinelibrary.com]

which previously led to the declaration of a fatigue limit, but beyond this regime, another significant decrease in fatigue strength was observed. This behavior was characterized by a duplex S–N approach, which incorporated a S–N curve for surface-induced failure S_f and another for internal failure initiation I_f.[28] Depending on the material, four different types can exist, which are shown in Figure 7. Therein, the Stüssi S–N curve was chosen to model the surface-induced failure, since it well represents the results in this work, while the internal damage initiation S–N curve is represented by a straight line (Basquin approach). According to Shiozawa et al[28] the four types are as follows:

A. surface failure dominated fatigue life
B. surface failure up to the VHCF regime followed by a distinct change to internal damage initiation
C. mixture of surface and internal damage initiation
D. internal failure dominated fatigue life

Although this concept was derived from experiments with metal alloys, it is expected to be transferable to polymers, as the same holds for nearly all S–N models. However, the experimental results from this work are rather limited concerning (very) high cycle data, since there

were only five specimens in total with more than 10^6 cycles. Therefore, it is not known which gigacycle type is valid for the adhesive. Hence, the Haibach extension[32] to the VHCF regime was combined with the Stüssi S–N curve. The Haibach extension is based on an assumed continuation of the S–N curve in the VHCF regime with a slope

$$k_{ext} = 2k - 1, \quad (6)$$

where k is the slope within the high cycle fatigue regime and the slope of the Basquin line, respectively. Equation (6) can also be rewritten using the curve fitting parameter β of the Basquin model resulting in

$$\beta_{ext} = \left(\frac{2}{\beta} + 1\right)^{-1}. \quad (7)$$

Using this extension in combination with the Stüssi approach, the very good fit of the Stüssi S–N curve can be utilized up to the high cycle fatigue regime and a rather conservative approach is made for VHCF. Since the transition point of the Stüssi S–N curve to the extension line is chosen in such a way that the slope of the Stüssi S–N

curve matches the one of the extension line, the transition is smooth and does not require a decision on where the extension should start in terms of a stress or cycle threshold. The derived Stüssi–Haibach S–N curves are included in Figure 5, and the additional parameter set is shown in Table 2.

Note that in case future experiments reveal that the adhesive is a type B material, there is a chance that the Haibach extension line crosses the I_f-line, which could lead to non-conservative fatigue life predictions. However, this would most probably be the case at very small stress amplitudes and very high cycle numbers. With the use of proper safety factors, this risk is expected to be tolerable, given the alternatives of trusting the fatigue limit theorem with limited data or using the very conservative Basquin approach. However, further tests in the VHCF regime are required to distinctly identify the best-fit S–N model in a probabilistic manner, as limited data and scatter at very high cycles to failure do not yet allow a final conclusion.

3.5 | Apparent yield strength separation points

Sigmoidal-shaped S–N models such as the ones from Stüssi[25] and Kohout and Věchet[26] incorporate the ultimate static strength. Motivated by the very good fit of both models to the data, a comparison of static and fatigue data was done for different yield strengths, which were determined in a previous publication.[20] These are the following:

1. $\sigma_{y,0.2}$ - traditional yield strength at a plastic offset strain of 0.2% (2000 μm/m)
2. σ_y - derivative-based yield strength according to Christensen[33,34]
3. $\sigma_{y,0.01}$ - surrogate proportional limit at a plastic offset strain of 0.01% (100 μm/m)

In case of the shear-based S–N curve, the respective plastic offset strains have to be converted to the equivalent stress-strain space, which was done using the experimental (strain) yield locus in combination with an elliptical scaling approach.[20]

The comparison of the static stress-strain curves (true stresses and strains) and the S–N results is shown in Figure 8. Note that the ordinate of the axial S–N curves in Figure 8 shows the maximum stress and not the amplitude; hence, the $R = 0$ curve is above the $R = -1$ curve. In addition, the strain rate in the static tests was different from the strain rate in the S–N tests. Thus, the comparison is affected by the viscoelasticity of the adhesive.

However, due to the low temperature increase in the experiments and the test frequency adaption on each load level, compare Table 1, this influence was minimized as much as possible.

It was found that $\sigma_{y,0.2}$ can be approximated as the upper separation point of the Basquin- and Stüssi S–N curves. While this approximation is quite accurate for the axial S–N curves of this work, it is a rough estimation for torsion. The surrogate proportional limit $\sigma_{y,0.01}$ is very close to the apparent fatigue limit σ predicted by the Stüssi S–N curve for both axial and torsional data at $R = -1$. However, at $R = 0$, this is not the case for the recorded data. The derivative-based yield strength σ_y might serve as a rough estimation for the lower separation point of the Basquin- and Stüssi S–N curves for axial fatigue tests; however, this does not apply for torsion.

While these findings are not decisive enough to derive general rules, they can still serve as useful first approximations. For instance, during the experimental determination of a S–N curve, only one load level is necessary for a Stüssi S–N curve fit if the ultimate strength and the surrogate proportional limit $\sigma_{y,0.01}$ are used as asymptotes. This is expected to help with specimen allocation and planning of test machine occupancy.

3.6 | Comparison with literature

Publicly available information on the coupon level fatigue behavior of the rotor blade adhesive investigated in this work is limited to two publications[9,10] in terms of S–N data. For a fair comparison, the specimen geometry and stress ratio should be as similar as possible. Therefore, Fernandez et al[9] is used for a comparison, since Sears et al[10] relied on lap shear tests. To account for similar stress ratios, only the torsional fatigue data of this work can be compared with Fernandez et al[9] as both were recorded at $R = -1$. The fatigue data presented in Fernandez et al[9] were normalized using the measured static shear strength. However, as the shear strength was calculated based on the purely elastic torsional formulae, it needs to be corrected, because the material was proven to exhibit significant plasticity.[20] The apparent brittle behavior of the tests in Fernandez et al[9] is hence attributed to a high porosity level, whereas the material surrounding the pores exhibited significant plastic strains.[20] Therefore, the purely plastic formulae result in a more realistic estimation of the shear strength. A correction factor of $\tau_{pl} = 0.873 \cdot \tau_{el}$ was identified to account for this issue in a previous publication.[20] A deduction of the correction factor and a detailed discussion on elasto-plastic shear stresses in torsion tests can be found therein.
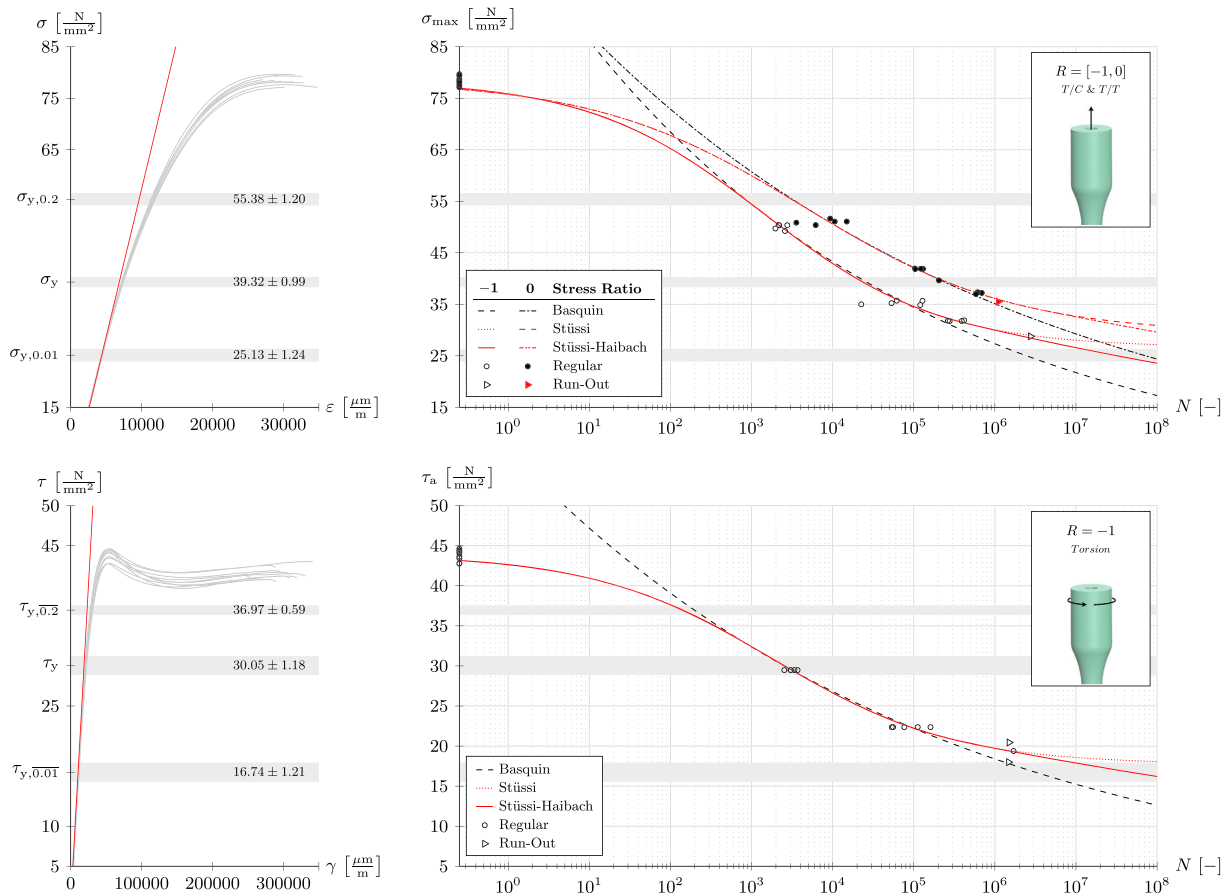
FIGURE 8 Comparison of static (true) stress–strain curves with experimental fatigue results and corresponding S–N curve fits. Static results represent the tensile and torsion test carried out in a previous publication.[20] Gray horizontal bars represent different yield point definitions including their standard deviation. [Colour figure can be viewed at wileyonlinelibrary.com]
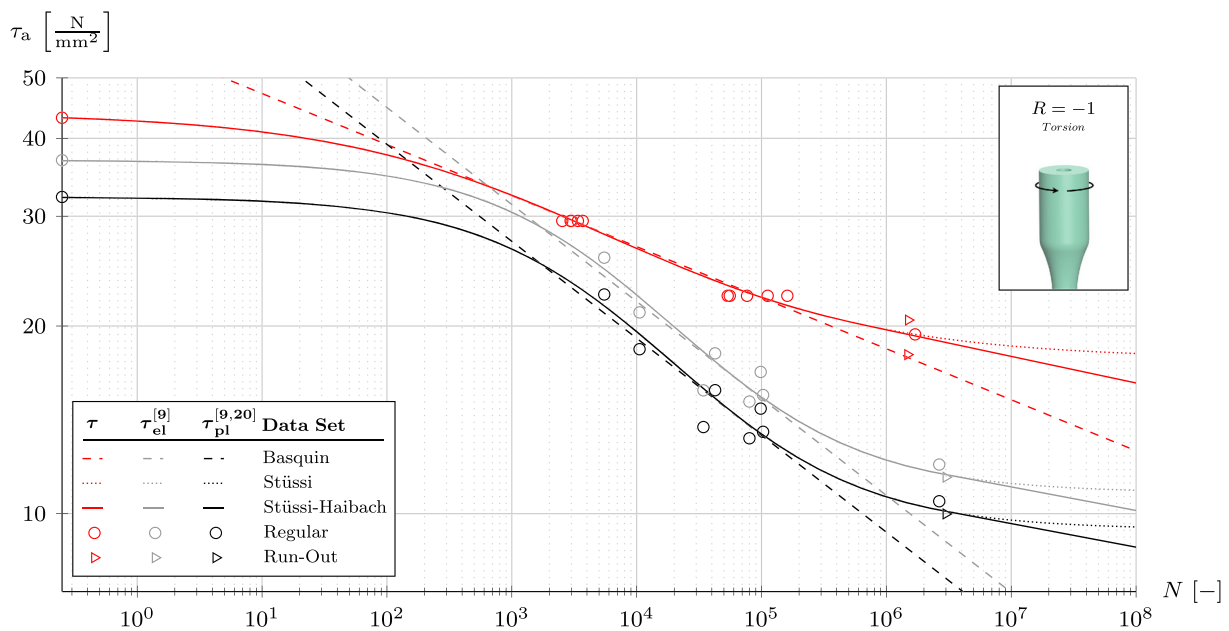

FIGURE 9 Comparison of torsional S–N results. The data set of this work is labeled τ, while data from Fernandez et al[9] are labeled τ_{el} and τ_{pl}. The latter was altered with a correction factor, which was derived in a previous publication.[20] A high porosity level in the specimens of Fernandez et al[9] is interpreted as the main reason for the reduced fatigue performance in comparison with this work. [Colour figure can be viewed at wileyonlinelibrary.com]

The differences between the measurements presented in Fernandez et al[9] and this work are shown in Figure 9. The linear elastic results stated in Fernandez et al[9] are shown in gray, while the results including the mentioned correction are shown in black. Both versions show significantly reduced fatigue properties in comparison with the results of this work. Possible uncertainties related to the conversion of the displacement-controlled tests to load-controlled tests in this work, compare Section 3.2, are not expected to affect this, as the differences between the results are too large. In fact, neglected strain rate effects in the conversion, compare Section 3.2, are expected to result in a conservative estimation of this works' S–N curve. Therefore, it can be confirmed that the porosity level and the underlying manufacturing methods have a very significant impact.

The differences between both measurement campaigns are also load level-dependent. A constant safety factor to account for manufacturing defects in general is therefore not recommendable regarding the permissible amplitude or cycles to failure. However, a safety factor applied to the slope of the S–N curve seems to be a reasonable simplification. It must be noted that different tempering cycles and orientations of the reinforcement fibers can also contribute to the discussed differences in fatigue performance. Especially the orientation of the reinforcement fibers is likely to influence fatigue life since it can affect microscale and mesoscale crack orientations.[35] More detailed analyses are required to estimate the individual contribution of the porosity level, tempering, and fiber orientation in terms of material properties and safety factors. However, the porosity level is interpreted as the main reason for the differences in fatigue performance as similar load level-dependent observations have been made for various metallic alloys with different levels of porosity in literature.[36–38]

Despite the differences in fatigue performance shown in Figure 9, the Stüssi (or Stüssi–Haibach) S–N model fits the data very well. The same was found by Rosemeier and Antoniou[39] and Rosemeier et al[40] for other epoxy-based resins/adhesives. However, as the VHCF scatter remains unknown in the aforementioned publications, it is still required to verify S–N models in this regime on a statistical basis, compare Section 3.4.

4 | STIFFNESS DEGRADATION

The stiffness degradation measurements were done alongside the fatigue tests according to Figure 3. Since the degradation of the Young's and shear modulus was measured independently of the active load type (axial or torsional), biaxial interactions could be analyzed.

4.1 | Cycle- and load-dependent modeling

The relative degradation is calculated as the ratio of the current modulus, which is a function of the cycle number n, and the initial modulus. The moduli are assumed to be linearly proportional to the measured load-displacement curves. This results in

$$E \propto \frac{dF}{du}, G \propto \frac{dT}{d\psi}, \quad (8)$$

$$\tilde{E}(n) = \frac{E(n)}{E_0} \cdot 100, \tilde{G}(n) = \frac{G(n)}{G_0} \cdot 100, \quad (9)$$

where E is the Young's modulus, G is the shear modulus, F and T are axial force and torque, and u and ψ are axial displacement and rotation.

The degradation model is set up with the normalized cycle count $\tilde{N}$ and normalized load level $\tilde{L}$ given by

$$\tilde{N} = \frac{n}{N}, \tilde{L} = \frac{\sigma_a}{R_m}. \quad (10)$$

In case of the torsional S–N tests, $\tilde{L}$ is defined by the ratio between the shear stress amplitude τ_a and the static shear strength, respectively.

Independent of the load type, it was found that the adhesive shows a rapid degradation of E and G during the first 5%–10% of fatigue life followed by a slower and approximately linear decline afterwards; see Figure 10 (black solid lines). A good fit of the recorded degradation is provided by a power law given by

$$\tilde{E} = 100 - A\tilde{N}^B, \quad (11)$$

where A and B are curve fitting parameters. The same model is also used for the G modulus degradation.

The overall degradation was found to be load level-dependent. However, an extrapolation of the data is difficult on account of the limited data set. Therefore, a conservative approach is chosen. Concerning a stress-based fatigue life analysis, a conservative approach represents the assumption of a low stiffness degradation in VHCF. This is because a stiffness degradation will lead to lower stresses and hence longer fatigue life. Therefore, it is

assumed that the stiffness degradation tends to zero at very small load amplitudes. Note, however, that in some engineering applications, an overestimation of the stiffness degradation might be a more conservative design approach than to neglect it. The tower clearance of wind turbine rotor blades could be such a case depending on the rotor blade design. Therefore, the extrapolation in

this work must be treated with caution, although the contribution of adhesive to the overall stiffness of a structure will most likely be small.

Given the assumption explained above, it is further assumed that the parameters A and B are load level-dependent and can be described by rational functions with a polynomial degree of 1 in the numerator and a
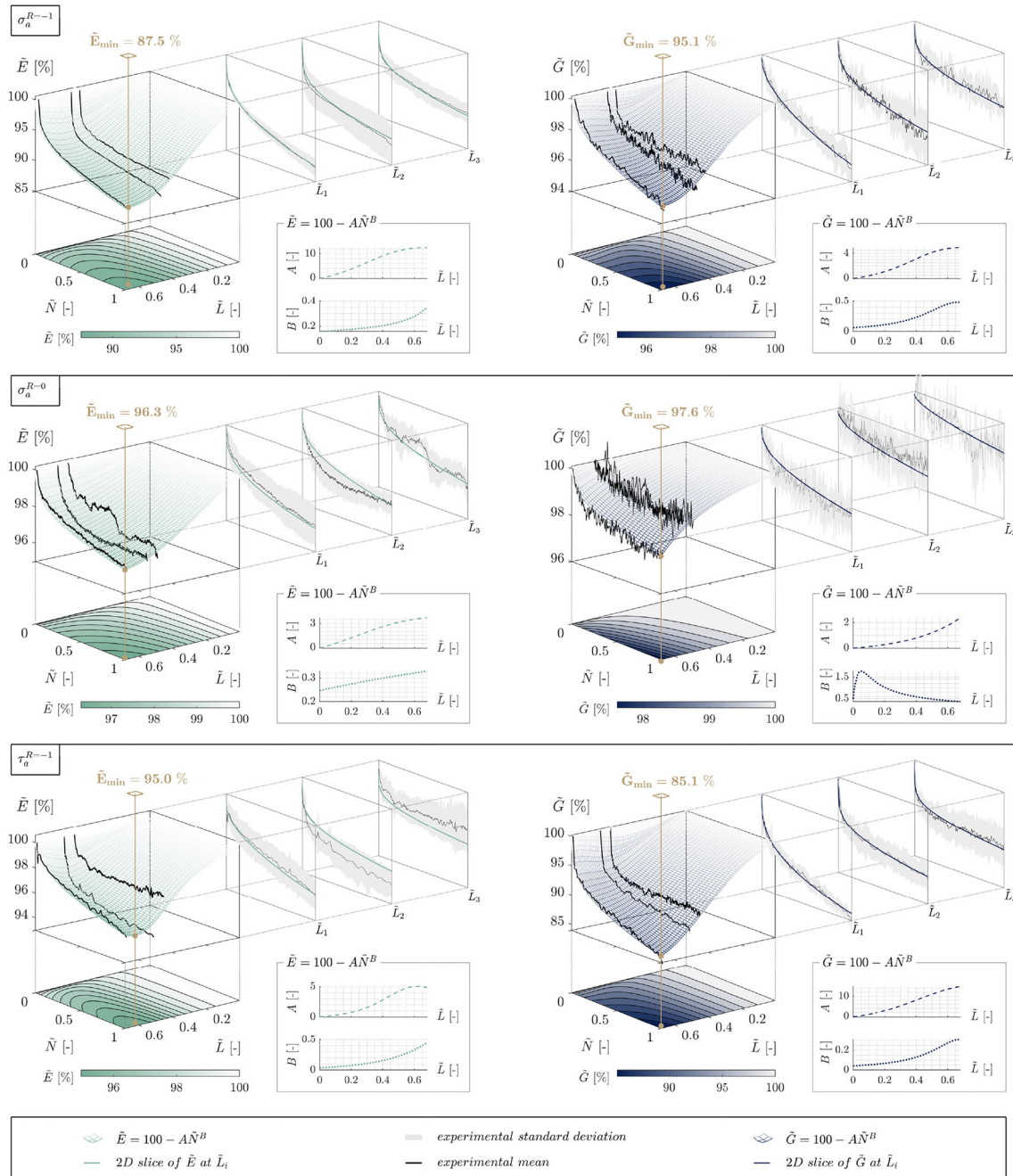

FIGURE 10 Modeling of the relative stiffness degradation in tension/compression ($\sigma_a^{R=-1}$), tension/tension ($\sigma_a^{R=0}$) and torsion ($\tau_a^{R=-1}$). A power law is used to model the data as a function of the normalized cycles to failure $\tilde{N}$. The fitting parameters of the power law (A and B) were found to be rational functions of the normalized load level $\tilde{L}$. The respective functions of $A(\tilde{L})$ and $B(\tilde{L})$ are shown in inserted boxes. A comparison of the model prediction (colored) and the experimental mean (black) is given in 2D slices at each investigated load level ($\tilde{L}_1, \tilde{L}_2, \tilde{L}_3$) showing good agreement. Fitting parameters are given in Table 3. [Colour figure can be viewed at wileyonlinelibrary.com]

polynomial degree of 2 in the denominator such as the following:

$$A = \frac{p_1 \tilde{L} + p_2}{\tilde{L}^2 + q_1 \tilde{L} + q_2}, B = \frac{p_3 \tilde{L} + p_4}{\tilde{L}^2 + q_3 \tilde{L} + q_4}, \quad (12)$$

where p_1 to p_4 and q_1 to q_4 are curve fitting parameters. Based on this, the overall degradation functions depend on eight curve fitting parameters in addition to the respective ultimate static strength R_m.

To simplify the rational function fits of A and B, load-dependent smoothing splines were modeled in an intermediate step, which connected the recorded data points and the assumed zero degradation line at zero load. A complete degradation curve could thus be derived for each $\tilde{L}$, which was fitted with a power law according to Equation (11). This way, a smooth relationship between the power law fitting parameters A and B and the normalized load level $\tilde{L}$ was generated. Therefore, enough data points were provided for the rational function fit of A and B, which are shown in Figure 10 (2D plots with grid) and Table 3. Given the adaptability of rational

function fits, the overall degradation model is very adaptable while the number of fitting parameters is still manageable.

The overall fit of the model to the measured data can be evaluated based on the 2D slices given in Figure 10. These depict the mean (black) and standard deviation (gray) of the experimental data in comparison with the model (colored). A good fit is provided for each load type. Since the experimental standard deviation is quite large, the upper and lower standard deviations were also modeled as offset-functions in the same way as the mean values. This way, the residual fatigue life prediction of run-out specimens, compare Section 4.3, includes the possibility of an uncertainty analysis. The additional fitting parameters are included in Table 3.

The degradation in the active load direction was found to be the largest in each test setup. For instance, if the adhesive is subjected to an axial $R = -1$ load, the E modulus is reduced to 87.5%, while the G modulus is reduced to 95.1% on account of the axial load. This can be interpreted as a confirmation of the anisotropic behavior of the adhesive and an oriented crack growth during the experiments. Interestingly, the degradation at an

TABLE 3 Fitting parameters of the mean stiffness degradation functions (μ) with additional parameter sets for a positive (μ^+) and negative (μ^-) standard deviation offset, respectively.

Load type	Model	A [−]				B [−]			
		p_1 [−]	p_2 [−]	q_1 [−]	q_2 [−]	p_3 [−]	p_4 [−]	q_3 [−]	q_4 [−]
$\sigma_a^{R=-1}\|\tilde{E}$	μ^+	13.2392	−0.3163	−0.9134	0.9234	25.3665	−0.7556	100.0000	−1.2308
	μ	6.2867	−0.1225	−0.8265	0.4323	−10.3208	13.7304	−99.9999	86.7407
	μ^-	6.9112	−0.1613	−0.7964	0.3996	22.8418	−0.8368	100.0000	−1.2227
$\sigma_a^{R=-1}\|\tilde{G}$	μ^+	4.6684	−0.4116	−1.0753	0.9467	−11.1194	18.1751	−100.0000	84.7842
	μ	1.6602	−0.0210	−1.0089	0.4498	0.0003	0.0309	−1.3263	0.5048
	μ^-	2.5925	0.1159	−0.9686	0.5137	41.9786	6.6405	−26.8563	100.0000
$\sigma_a^{R=0}\|\tilde{E}$	μ^+	1.3670	−0.0586	−0.7755	0.3844	0.8300	−0.0236	1.5492	−0.0756
	μ	3.5008	−0.0492	−0.6917	0.6369	23.4480	24.6517	33.6168	100.0000
	μ^-	7.1944	−0.0094	−0.7435	1.0786	28.1620	0.3035	100.0000	6.1375
$\sigma_a^{R=0}\|\tilde{G}$	μ^+	0.2683	−0.0908	−1.4663	0.5899	0.0517	−0.0124	−0.7269	0.1330
	μ	1.9030	−0.0193	−2.5075	1.7758	0.2650	0.0017	0.0496	0.0035
	μ^-	100.0000	2.7864	−30.9189	43.1881	0.1571	0.0019	−0.1192	0.0445
$\tau_a^{R=-1}\|\tilde{E}$	μ^+	0.9033	−0.0849	−1.1623	0.4670	−0.0721	0.0093	−0.8627	0.0705
	μ	0.7141	0.0132	−1.0914	0.3829	0.0769	0.0380	−1.9315	1.0528
	μ^-	1.5705	−0.0010	−0.9956	0.3895	36.0028	6.5741	1.8603	100.0000
$\tau_a^{R=-1}\|\tilde{G}$	μ^+	7.8089	−0.4494	−1.5464	0.9363	−0.0390	0.0329	−1.4448	0.5381
	μ	7.3408	−0.2099	−1.1399	0.6338	−0.0137	0.0225	−1.3975	0.5308
	μ^-	7.0820	−0.1529	−0.9809	0.4960	20.2098	7.2870	−23.9835	100.0000

Note: To avoid replication errors, all digits should be used.

active torsional $R = -1$ load approximately mirrors the degradation with an active axial load at the same stress ratio, resulting in a G modulus reduction to 85.1% and a E modulus reduction to 95.0% based on the active torsional load.

In comparison, the degradation at an active axial $R = 0$ load is the smallest. Since this load type also has the smallest load amplitudes, it is concluded that the load amplitude is governing the stiffness degradation and not the maximum load resulting from the combination of mean load and amplitude. Hence, a mean load reduces the fatigue life of the adhesive but does not increase stiffness degradation.

As the stiffness degradation is non-linear in each case, these measurements might serve as a basis to include sequence effects in the fatigue life prediction. The validation of a possibly non-linear damage accumulation can, however, not be done with this work's uniaxial fatigue tests. Upcoming biaxial fatigue tests will provide more possibilities in this regard.

Further experiments are required to validate the stiffness degradation model in the VHCF regime. Strain rate-related differences of the respective load levels were minimized by an adaption of the test frequency in the S–N tests, compare Section 2.2.

4.2 | Comparison with residual strength tests

In case a run-out was declared, a residual strength test (RST) was performed. Strain gauge rosettes, identical to the ones used in the previously carried out static tests,[20] were applied to most of the run-out specimens for these tests. Hence, the employed force- and displacement-based stiffness degradation measurement could be validated by comparison of the accumulated degradation of the fatigue test and the stiffness measurement of the RST. The degradation identified by these methods was found to be different by approximately $\tilde{E} - \tilde{E}_{\text{RST}} \approx 0.5\%$ and $\tilde{G} - \tilde{G}_{\text{RST}} \approx 2\%$. In all cases, the stiffness degradation measured in the RSTs was smaller than the last measurement in the fatigue test. Therefore, these deviations are expected to be influenced by viscoelastic recovery effects of the adhesive,[20] because the specimen instrumentation and preparation for the RSTs took time. This would also explain the larger difference in torsion, since the viscoelastic recovery was found to be faster in this case.[20] Independent of viscoelastic effects, the results of the employed fatigue stiffness degradation measurement method are close to the instrumented RSTs, confirming the validity of the method. An influence of testing machine compliance was not identified and therefore neglected.

In addition, the residual strength tests were compared with regular static tests. In Figure 11, a comparison between the static tensile test from a previous publication[12,20] and the RST of run-out specimen 174 is shown at the top. This specimen withstood $2.76 \cdot 10^6$ cycles at a fully reversed axial load of 28.79 N/mm², and yet the ultimate strength is about 4.0% higher than the average of the static tensile test. At the same time, the Young's modulus decreased by 5.8%. Given the very low scatter of the static tests and the well-controlled manufacturing process in general,[12] the strength difference is more likely to be phenomenological than coincidence. While the stiffness degradation is attributed to cyclic matrix softening, the increase in strength is linked to strain hardening. Interestingly, the post-fatigue strain hardening was more significant than in the regular static tests. A potential reorientation of the polymer chains or the reinforcement fibers could contribute to this effect, although this is also expected to happen in the static tests. However, due to the matrix softening in fatigue, the reorientation could have been more significant than in the regular static tests. A more general interpretation is that accumulated (small scale) damage during fatigue alleviates stress
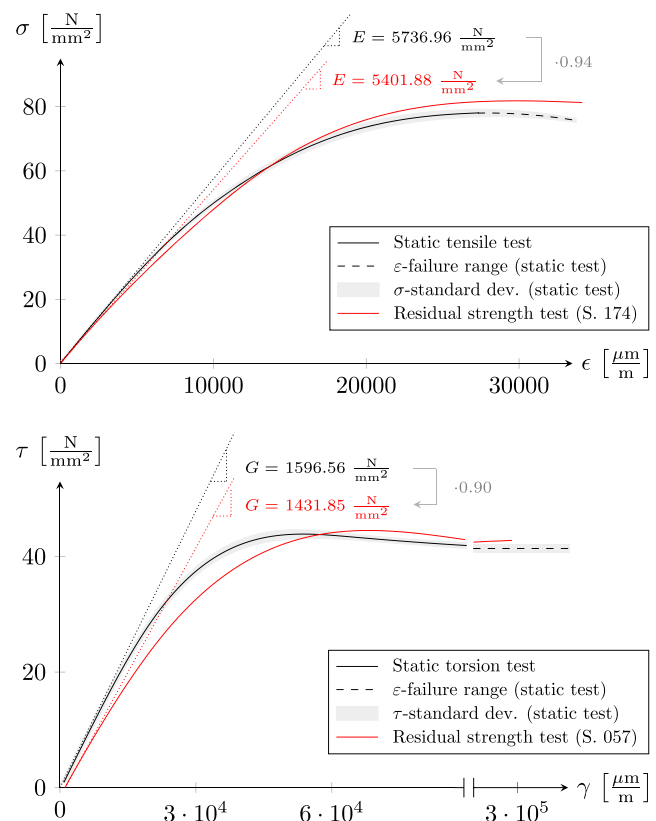

FIGURE 11 Residual strength test for run-out specimen 174 (tested in tension/compression loading at $R = -1$) and run-out specimen 057 (tested in torsional loading at $R = -1$). Static test data were taken from previous publications.[12,20] [Colour figure can be viewed at wileyonlinelibrary.com]
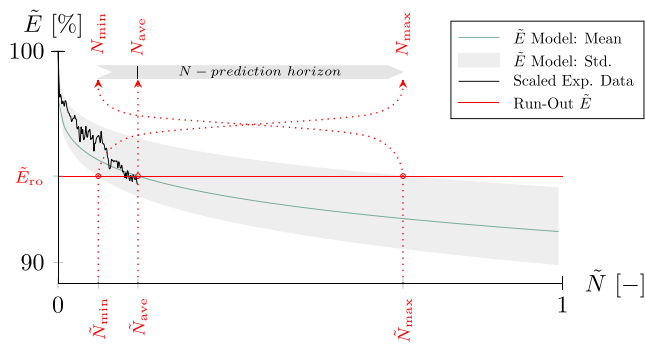
FIGURE 12 Stiffness degradation-based fatigue life estimation of run-out specimen 174 using the $\tilde{E}$ model and it's standard deviation. Intersections of the last measured degradation $\tilde{E}_{ro}$ with the $\tilde{E}$ model lead to a predicted fatigue life horizon. [Colour figure can be viewed at wileyonlinelibrary.com]

concentrations,[41] which in turn may allow for a higher ultimate strength in a post-fatigue test.

Figure 11 also shows the RST of specimen 057, which was tested in fully reversed torsion up to $1.5 \cdot 10^6$ cycles. In this case, the ultimate strength difference is insignificant at about 1%, while the stiffness degraded by approximately 10%. The torsional RST appears as a delayed version of the regular static test, and a potential (additional) reorientation effect concerning the ultimate strength was not significant.

Further experimental validation of the fiber reorientation hypothesis is necessary.

4.3 | Run-out fatigue life estimation

Based on the load level and the accumulated stiffness degradation of the run-out specimens, a residual fatigue life estimation is possible. Given the limited data, their standard deviation, and the assumptions used to model the stiffness degradation, these predictions have to be understood as rough estimations.

The residual life estimation is schematically shown in Figure 12 for specimen 174. The degradation functions are evaluated at the respective load level of the run-out specimen. Subsequently, the intersection points of the model with the last recorded degradation value ($\tilde{E}_{ro}$) are calculated. In case the measurement was noisy, a direct power law fit of the experimental data can also be used to extract a smoothed $\tilde{E}_{ro}$ value. Note that the first intersection point $\tilde{N}_{min}$ corresponds to the maximum of the fatigue life prediction N_{max}, because the potential minimum of used cycles implies a maximum of residual cycles to failure. The absolute cycles to failure can be found as the inverse of the intersection points multiplied by the run-out cycles of the specimen, for example,

TABLE 4 Stiffness degradation-based fatigue life estimation of run-out specimens.

Specimen no.	N_{min} [−]	N_{ave} [−]	N_{max} [−]
174	4,036,622	17,420,943	34,629,862
057	−	−	−
166	1,480,000	8,462,946	21,467,943

$$N_{ave} = \frac{*(N)}{\tilde{N}_{ave}}. \tag{13}$$

When this is done for all intersection points, a prediction horizon can be calculated, compare Figure 12. The resulting fatigue life horizons for all run-out specimens are shown in Figure 5 and Table 4. In case of specimen 057, no intersection point was found, as the degradation of this specimen was even below the lower standard deviation of the model. Therefore, the fatigue life prediction was not applicable for this specimen. However, in case of specimen 174 and 166, the predicted life span is in good agreement with the Stüssi–Haibach S–N curve with respect to the expected standard deviation of S–N tests. It is emphasized that the stiffness degradation model is independent of the S–N fits. Therefore, the agreement of the fatigue life prediction horizons with the, for example, Stüssi–Haibach S–N curve can be interpreted as indications of their validity.

A qualitative verification of the prediction is provided by a comparison of the stiffness degradation model and the scaled experimental time series. In Figure 12, this is shown based on the mean intersection point of the stiffness degradation model, so that the run-out cycles $*(N)$ of this specimen were scaled to $\tilde{N}_{ave}$. A reasonable agreement between the scaled experimental results and the model was found. The mean intersection point was therefore highlighted by a vertical black line in the fatigue life prediction horizon as the most probable result, compare Figures 12 and 5.

Theoretically, this approach can be applied to both the E and G modulus degradation measurement to gain a broader picture of the uncertainties. However, in this work, the stiffness degradation-based fatigue life estimation is solely done using the measurement from the active load component, as these data were in better agreement with the respective models and the overall degradation was more significant.

5 | CONCLUSION

Axial and torsional fatigue tests were carried out for a structural rotor blade adhesive at different stress ratios.

The specimens utilized for the experiments were optimized in a previous study in such a way that manufacturing-induced defects are minimized. This resulted in significantly improved fatigue properties in comparison to hand-mixed specimens with high porosity. This highlights the significance of the manufacturing process in terms of the reliability of the material properties, as low-quality specimens will lead to (very) conservative estimates and potentially wrong conclusions concerning the material modeling.

The Stüssi S–N approach was found to be an excellent fit of the data for all investigated stress ratios and load types. On account of recent gigacycle fatigue studies and the lack of data for the adhesive in this regime, a conservative engineering approximation was derived including a smooth transition of the Stüssi S–N curve to the Haibach extension line.

Based on the good fit of the sigmoidal-shaped Stüssi S–N curve and the very significant and load level-dependent differences of the results to hand-mixed specimens, a constant safety factor for manufacturing-induced defects in terms of permissible amplitude or cycles to failure does not seem recommendable. Instead, a safety factor related to the slope of the S–N curve was identified as a more appropriate option.

A comparison of the static (true) stress–strain curves and the S–N data indicated that a surrogate proportional limit at a plastic offset strain of 100 µm/m may serve as a first approximation of the fatigue limit prediction by the Stüssi S–N line. While this fatigue limit is not trustworthy for gigacycle fatigue applications without sufficient experimental data, this approximation can still be useful for the allocation of specimens and testing equipment in the high cycle fatigue regime.

The experiments were accompanied by stiffness degradation measurements. It was found that the degradation of the stiffness moduli is load level-dependent and in between 5% and 15%. A smooth function fit of the data was generated employing a power law fit with load level-dependent fitting parameters. The model was applied to predict the residual fatigue life of run-out specimens. In addition, the driving factor for stiffness degradation was identified to be the stress amplitude, as a mean stress did not accelerate the degradation process.

AUTHOR CONTRIBUTIONS

Michael Kuhn: Development and implementation of the proposed methods, post-processing of the µCT scan segmentation, and illustrations and writing of the paper. **Nikolas Manousides:** High-resolution X-ray microscopy (µCT scanning) of the specimens and segmentation pre-processing. **Alexandros Antoniou:** Scientific advice and support with executing the experiments at Fraunhofer IWES. **Claudio Balzani:** Conceptual guidance and scientific supervision of all project phases.

CONFLICT OF INTEREST

The authors declare no potential conflict of interests.

DATA AVAILABILITY STATEMENT

The raw/processed data required to reproduce these findings cannot be shared at this time due to legal or ethical reasons.

ORCID

Michael Kuhn https://orcid.org/0000-0002-5859-5444

REFERENCES

1. Noever-Castelos P, Haller B, Balzani C. Validation of a modeling methodology for wind turbine rotor blades based on a full-scale blade test. *Wind Energy Sci*. 2022;7:105-127.
2. Sayer F, Antoniou A, van Wingerde A. Investigation of structural bond lines in wind turbine blades by sub-component tests. *Int J Adhes Adhes*. 2012;37:129-135.
3. Subrahmanian KP, Dubouloz F. Adhesives for bonding wind turbine blades. *Reinf Plast*. 2009;53:26-29.
4. Caous D, Bois C, Wahl J-C, Palin-Luc T, Valette J. Analysis of multiaxial cyclic stress state in a wind turbine blade. 20th ICCM; 2015.
5. Rommel DP, Di Maio D, Tinga T. Calculating wind turbine component loads for improved life prediction. *Renew Energ*. 2020;146:223-241.
6. Rosemeier M, Krimmer A, Bardenhagen A, Antoniou A. Tunneling Crack Initiation in Trailing-Edge Bond Lines of Wind-Turbine Blades. *AIAA J*. 2019;57:5462-5474.
7. Noever-Castelos P, Ardizzone L, Balzani C. Model updating of wind turbine blade cross sections with invertible neural networks. *Wind Energy*. 2022;25:573-599.
8. Sayer F, Antoniou A, Goutianos S, Gebauer I, Branner K, Balzani C. ReliaBlade Project: A Material's Perspective towards the Digitalization of Wind Turbine Rotor Blades. *IOP Conf Ser: Mater Sci Eng*. 2020;942:12006.
9. Fernandez G, Vandepitte D, Usabiaga H, Debruyne S. Static and cyclic strength properties of brittle adhesives with porosity. *Int J Fatigue*. 2018;117:340-351.
10. Sears AT, Samborsky DD, Agastra P, Mandell JF. Fatigue Results and Analysis for Thick Adhesive Notched Lap Shear Test. In: Proc. AIAA; 2010.

11. Zarouchas D, Nijssen R. Mechanical behaviour of thick structural adhesives in wind turbine blades under multi-axial loading. *J Adhes Sci Technol*. 2016;30:1413-1429.

12. Wentingmann M, Manousides N, Antoniou A, Balzani C. Design and manufacturing optimization of epoxy-based adhesive specimens for multiaxial tests. *Mater Des*. 2021;212:110213.

13. Antoniou A, Rosemeier M, Tazefidan K, Krimmer A, Wolken-Möhlmann G. Impact of Site-Specific Thermal Residual Stress on the Fatigue of Wind-Turbine Blades. *AIAA J*. 2020;58:4781-4793.

14. Krogh L, Schawe JEK, Possart W. Dynamic mechanical properties of very thin adhesive joints. *J Appl Polym Sci*. 2015;132:42058.

15. Ries M, Possart G, Steinmann P, Pfaller S. A coupled md-fe methodology to characterize mechanical interphases in polymeric nanocomposites. *Int J Mech Sci*. 2021;204:106564.

16. Tokyo Measuring Instruments Laboratory Co., Ltd.. GFRAB-3-350-50. https://tml.jp/e/product/strain_gauge/gf_list.html, Accessed: October, 2022; 2021.

17. Hexion™. Technical Data Sheet - EPIKOTE™ Resin MGS™ BPR 135G-Series and EPIKURE™ Curing Agent MGS™ BPH 134G-137GF; 2021.

18. Carl Zeiss AG. Zeiss Xradia 410 Versa. https://www.zeiss.com/microscopy/int/products/x-ray-microscopy/zeiss-xradia-410-versa.html, Accessed: October, 2022; 2021.

19. Walter + Bai AG. Axial / Torsional Test Systems. https://www.walterbai.com/page/products/Materials_Testing_Systems/Axial-Torsional_Testing_System/index.php, Accessed: October, 2022; 2021.

20. Wentingmann M, Manousides N, Antoniou A, Balzani C. Yield surface derivation for a structural adhesive based on multiaxial experiments. *Polym Test*. 2022;113:107648.

21. Adden S, Horst P. Stiffness degradation under fatigue in multi-axially loaded non-crimped-fabrics. *Int J Fatigue*. 2010;32:108-122.

22. Wöhler A. Über die Versuche zur Ermittlung der Festigkeit von Achsen, welche in den Werkstätten der Niederschlesisch-Märkischen Eisenbahn zu Frankfurt a. d. O. angestellt sind. *Zeitschrift für Bauwesen*. 1863;13:233-258.

23. Basquin OH. The exponential law of endurance tests. *Am Soc Test Mater*. 1910;10:625-630.

24. Sendeckyj GP. Fitting models to composite materials fatigue data. *ASTM STP*. 1981;734:245-260.

25. Stüssi F. Zur Theorie der Dauerfestigkeit. *IABSE Congress Report*. 1956;5:229-234.

26. Kohout J, Věchet S. A new function for fatigue curves characterization and its multiple merits. *Int J Fatigue*. 2001;23:175-183.

27. Miner MA. Cumulative Damage in Fatigue. *J Appl Mech*. 1945;12:159-164.

28. Shiozawa K, Lu L, Ishihara S. S–N curve characteristics and subsurface crack initiation behaviour in ultra-long life fatigue of a high carbon-chromium bearing steel. *Fatigue Fract Eng M*. 2001;24:781-790.

29. Hong Y, Zhao A, Qian G, Zhou C. Fatigue strength and crack initiation mechanism of very-high-cycle fatigue for low alloy steels. *Metall Mater Trans A*. 2012;43:2753-2762.

30. Marines I, Bin X, Bathias C. An understanding of very high cycle fatigue of metals. *Int J Fatigue*. 2003;25:1101-1107.

31. Newman JCJ. Fatigue and Crack-Growth Analyses under Giga-Cycle Loading on Aluminum Alloys. *Procedia Eng*. 2015;101:339-346.

32. Haibach E. *Betriebsfestigkeit*: Springer-Verlag; 2006.

33. Christensen RM. Observations on the definition of yield stress. *Acta Mech*. 2008;196:239-244.

34. Christensen RM. *The Theory of Materials Failure*. Oxford University Press; 2016.

35. Rolland H, Saintier N, Raphael I, Lenoir N, King A, Robert G. Fatigue damage mechanisms of short fiber reinforced pa66 as observed in-situ synchrotron x-ray microtomography. *Compos Part B Eng*. 2018;143:217-229.

36. Biswal R, Zhang X, Syed AK, Awd M, Ding J, Walther F, Williams S. Criticality of porosity defects on the fatigue performance of wire + arc additive manufactured titanium alloy. *Int J Fatigue*. 2019;122:208-217.

37. Heuler P, Grimm J, Fuhrmann K, Troßmann T, Eulitz K-G. Influence of porosity and environmental impact on fatigue life of magnesium alloys. *Materialwiss Werkst*. 2008;39:694-701.

38. Mayer H, Papakyriacou M, Zettl B, Stanzl-Tschegg SE. Influence of porosity on the fatigue limit of die cast magnesium and aluminium alloys. *Int J Fatigue*. 2003;25:245-256.

39. Rosemeier M, Antoniou A. Probabilistic approach for the fatigue strength prediction of polymers. *AIAA J*. 2022;60:951-961.

40. Rosemeier M, Melcher D, Krimmer A, Wroblewski W, Antoniou A. Validation of crack initiation model by means of cyclic full-scale blade test. *J Phys Conf Ser*. 2022;2265:32045.

41. Curtis PT. Durability testing of polymer composites. In: Kelly A, Zweben C, eds. *Comprehensive Composite Materials*. Pergamon; 2000:163-182.